



Facile synthesis of hierarchical $\text{Na}_2\text{Fe}(\text{SO}_4)_2@\text{rGO}/\text{C}$ as high-voltage cathode for energy density-enhanced sodium-ion batteries

Ge Yao^a, Xixue Zhang^a, Yongliang Yan^a, Jiyu Zhang^a, Keming Song^a, Juan Shi^{a,b}, Liwei Mi^b, Jinyun Zheng^a, Xiangming Feng^{a,*}, Weihua Chen^{a,*}

^a Green Catalysis Center, and College of Chemistry, Zhengzhou University, Zhengzhou 450001, Henan, China

^b Center for Advanced Materials Research, Zhongyuan University of Technology, Zhengzhou 450007, Henan, China

ARTICLE INFO

Article history:

Received 22 February 2020

Revised 9 March 2020

Accepted 10 March 2020

Available online 17 April 2020

Keywords:

Sodium ion batteries

High-voltage cathode

Fe-based sulfates

Full cell

Hierarchical structure

ABSTRACT

Fe-based sulfates are ideal cathode candidates for sodium-ion batteries (SIBs) owing to their high operating voltage and low cost but suffer from the nature of poor power performance. Herein, a hierarchical porous $\text{Na}_2\text{Fe}(\text{SO}_4)_2@\text{reduced graphene oxide/carbon dot}$ ($\text{Na}_2\text{Fe}(\text{SO}_4)_2@\text{rGO}/\text{C}$) with low carbon content (4.12 wt%) was synthesized via a facile homogeneous strategy benefiting for engineering application, which delivers excellent sodium storage performance (high voltage plateau of 3.75 V, 85 mAh g⁻¹ and 330 Wh kg⁻¹ at 0.05 C; 5805 W kg⁻¹ at 10 C) and high Na⁺ diffusion coefficient (1.19×10^{-12} cm² s⁻¹). Moreover, the midpoint voltage of assembled full cell could reach 3.0 V. The electron transfer and reaction kinetics are effectively boosted since the nanoscale $\text{Na}_2\text{Fe}(\text{SO}_4)_2$ is supported by a robust cross-linked carbon matrix with rGO sheets and carbon dots. The slight rGO sheets sufficiently enhance the electron transfer like a current collector and restrain the aggregation, as well as ensure smooth ion channels. Meanwhile, the carbon dots in the whole space connect with $\text{Na}_2\text{Fe}(\text{SO}_4)_2$ and help rGO to promote the conductivity of the electrode. Ex-situ X-ray powder diffraction and X-ray photoelectron spectrometry analysis confirm the high reversibility of this sodiation/desodiation process.

© 2020 Science Press and Dalian Institute of Chemical Physics, Chinese Academy of Sciences. Published by Elsevier B.V. and Science Press. All rights reserved.

1. Introduction

Sodium-ion batteries (SIBs) are considered as one of important potential large-scale energy storage systems due to abundant available resources, economic efficiency and the similar electrochemistry to that of lithium-ion batteries [1–4]. However, it still faces huge challenges to achieve high performance and their practical applications until more appropriate electrodes are discovered to satisfy the demand of high energy density and long cycle life [5–7]. In a battery, the cathode is a critical factor in evaluating the battery performance and its cost accounts for more than 30% [8]. Therefore, as the cost- and performance-determining part, it is urgently expected to develop the high-operating-voltage cathode with rapid and stable sodium-ion migration.

A series of cathode materials have been proposed and are under study. Sodium metal oxides are one of the candidates recently, although these layer materials suffer from poor cycling stability as well as large volume changes [9–12]. Prussian blue analogs (PBAs) are another promising cathode materials with good electro-

chemical properties, except the low tap density and temperature instability [13,14]. Additionally, polyanionic compounds (NASICONs [15,16], olivine [17], fluorophosphates [18], sulfates [19,20] and pyrophosphate [21,22]) have been extensively discussed because they possess high safety and favorable long life span owing to their durable polyanion framework systems. Among them, resource-abundant Fe-based sulfates, such as $\text{Na}_2\text{Fe}(\text{SO}_4)_2$ [23], $\text{Na}_2\text{Fe}(\text{SO}_4)_2 \cdot 2\text{H}_2\text{O}$ [24], $\text{NaFe}(\text{SO}_4)_2$ [25], alluaudite $\text{Na}_2\text{Fe}_2(\text{SO}_4)_3$ [26], etc., are considered as most promising cathode materials for SIBs because of the merits of high operation voltage (3.0–3.8 V) owing to $\text{Fe}^{3+}/\text{Fe}^{2+}$ reversible redox couples and strong electronegativity and inductive effect of SO_4^{2-} group [27,28]. Moreover, they are synthesized at a lower temperature. However, the further development of Fe-based sulfates materials is seriously impeded with low ion/electron conductivity and therefore poor rate performance.

To solve these problems, effective strategies including carbon introducing and architecture engineering to increase conductivity and elevate the power performance have been employed to modify the Fe-based sulfates materials. For instance, Deng's group [29] constructed carbon nanofiber films to enhance the electrochemical performance of $\text{Na}_{2+2x}\text{Fe}_{2-x}(\text{SO}_4)_3$ with D_{Na^+} values of $10^{-12.2}$ to $10^{-13.9}$ cm² s⁻¹ (higher than the pristine, 10^{-16} cm²

* Corresponding authors.

E-mail addresses: fengxm@zzu.edu.cn (X. Feng), chenweih@zzu.edu.cn (W. Chen).

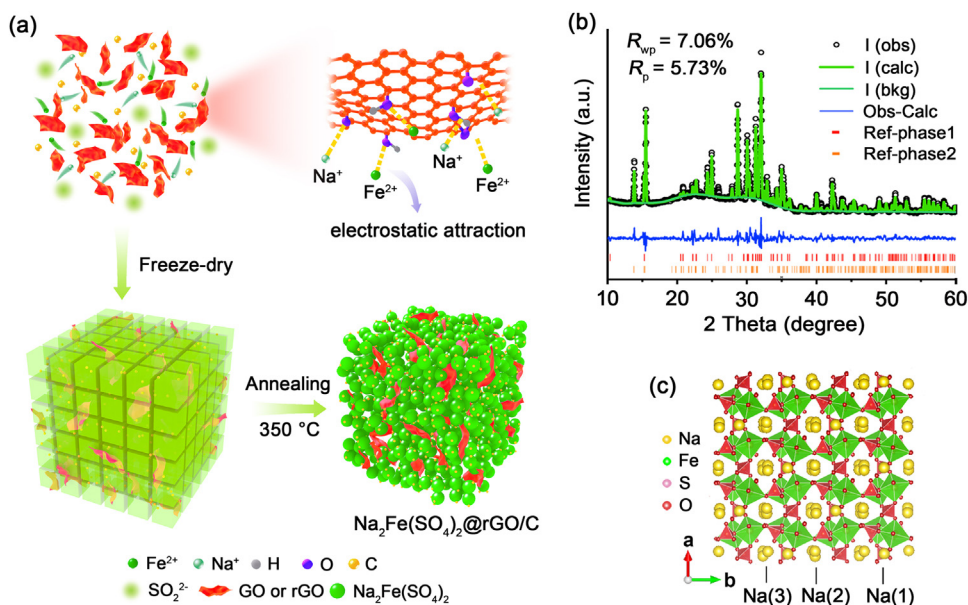


Fig. 1. Schematic illustration and Rietveld refinement XRD of $\text{Na}_2\text{Fe}(\text{SO}_4)_2@\text{rGO}/\text{C}$. (a) Schematic illustration of the preparation process of $\text{Na}_2\text{Fe}(\text{SO}_4)_2@\text{rGO}/\text{C}$. (b) Rietveld refinement of the powder XRD pattern of $\text{Na}_2\text{Fe}(\text{SO}_4)_2@\text{rGO}/\text{C}$, Ref-phase1: $\text{Na}_2\text{Fe}(\text{SO}_4)_2$, Ref-phase2: $\text{Na}_6\text{Fe}(\text{SO}_4)_4$. (c) Crystal structure of $\text{Na}_2\text{Fe}(\text{SO}_4)_2@\text{rGO}/\text{C}$.

s^{-1}) by a complex electrospinning and high-temperature calcination (1000°C) process, but with harmful reagents, including N, N-dimethylformamide and hydrofluoric acid solution. Liu and co-workers [30] reported the $\text{Na}_{2-2x}\text{Fe}_{2-x}(\text{SO}_4)_3\text{-G}$ compounds with high electronic conductivity and a D_{Na^+} value of $1.12 \times 10^{-14} \text{ cm}^2 \text{ s}^{-1}$ via graphene addition, superior to pristine ($4.10 \times 10^{-16} \text{ cm}^2 \text{ s}^{-1}$). Besides, the only reported $\text{Na}_2\text{Fe}(\text{SO}_4)_2/\text{C}$ by Pan's team [31] was designed with carbon-coating by using ascorbic acid as carbon source, with a carbon content of 10 wt% to deliver an enhanced voltage of 3.6 V but short cycle life (50 cycles). Thus, carbon modifying and architecture engineering are significant to improve the electrochemical performance. Though these strategies have acquired encouraging results, it should be noted that the improvement of ion/electron transport is still limited, and the cyclic and rate performance are undesirable; additionally, a complex operating process and dangerous reagents are always employed, highly blocking the commercial engineering production. To further accelerate the kinetics, the hierarchical nano conductive structure could be applied, owing to merits of a large contact area between the electrolyte and the active materials and sufficient ion/electron channels, to boost electrode performance. However, the successful achievement of hierarchical structure of Fe-based sulfates, facing the challenges of easy aggregation of polyanion structure and thermal instability of sulfate at high temperature, has not been reported yet. Therefore, attaining the effective hierarchical architecture design with simple routines could provide a chance to actually optimize the electrochemical performance and advance the practical application of Fe-based sulfates.

Herein, a hierarchical porous $\text{Na}_2\text{Fe}(\text{SO}_4)_2@\text{reduced graphene oxide}/\text{carbon dot}$ ($\text{Na}_2\text{Fe}(\text{SO}_4)_2@\text{rGO}/\text{C}$) was prepared via a facile and scalable homogeneous strategy with low cost and low energy consumption as high voltage cathode of SIBs. The introducing of rGO sheets urged the evenly electrostatic self-assembly process among carbon matrix and active materials, actualizing the cross-linked structure and inhibiting aggregation of $\text{Na}_2\text{Fe}(\text{SO}_4)_2$. The obtained robust hierarchical porous architecture could enable greatly boosted reaction kinetics with nano-sized $\text{Na}_2\text{Fe}(\text{SO}_4)_2$, smooth ion channels and facilitated electron transport in carbon matrix. The as-obtained $\text{Na}_2\text{Fe}(\text{SO}_4)_2@\text{rGO}/\text{C}$, with extremely low carbon content of 4.12 wt%, possesses high electrochemical per-

formance with high voltage plateau of 3.75 V, high capacity of 85 mAh g^{-1} at 0.05 C and stable cycling of 200 cycles, superior than the reported $\text{Na}_2\text{Fe}(\text{SO}_4)_2$ cathode [31]. The sodium storage mechanism and surface chemistry during operation are intensively studied via ex-situ X-ray powder diffraction (XRD) and X-ray photoelectron spectrometry (XPS). And the full cell application is successfully carried out with hard carbon as anode.

2. Results and discussion

The synthesis process of the hierarchical $\text{Na}_2\text{Fe}(\text{SO}_4)_2@\text{rGO}/\text{C}$ is illustrated in Fig. 1(a). The homogeneous solution was formed with Fe^{2+} , Na^+ , SO_4^{2-} , graphene oxide (GO) and carbon dots in deionized water, where positive charged Fe^{2+} and Na^+ were adsorbed on the surface of the GO sheets with electron-rich functional groups to achieve the in-situ self-assembly [32]. After freeze-dried, the obtained precursor was annealed in Ar atmosphere at 350°C , in which the crystal phase of sodium ferrous sulfate was formed and the GO was reduced to rGO sheets. The finally obtained composite shows an even robust cross-linked conductive carbon matrix, with rGO sheets and carbon dots, well supporting the nanoscale $\text{Na}_2\text{Fe}(\text{SO}_4)_2$. In this facile architecture design, the rGO sheets could enhance the electronic conductivity like a current collector while inhibiting the aggregation of $\text{Na}_2\text{Fe}(\text{SO}_4)_2$ as well as providing the smooth ion transfer channels. In addition, the carbon dots ensure the well-connection of $\text{Na}_2\text{Fe}(\text{SO}_4)_2$ particles and further enhance the conductivity. The precursor after freeze-drying was analyzed as $\text{Na}_2\text{Fe}(\text{SO}_4)_2 \cdot 4\text{H}_2\text{O}$, shown in Fig. S1(a). And this homogeneous synthesis process is extremely facile compared to various reported cathodes of SIBs in literature (Table S1), benefiting the engineering application.

XRD pattern of as-synthesized $\text{Na}_2\text{Fe}(\text{SO}_4)_2@\text{rGO}/\text{C}$ and its Rietveld refinement were shown in Fig. 1(b). The calculated pattern accords well with the observed profile, with R_{wp} (7.06%) and R_{p} (5.73%) lying in a reasonable range, which fits into the C2/c space group with the lattice parameters $a = 12.6732 \text{ \AA}$, $b = 12.7901 \text{ \AA}$, $c = 6.5302 \text{ \AA}$, $\beta = 115.5636^\circ$ and $V = 954.8724 \text{ \AA}^3$, and it was found to be isostructural to alluaudite-type $\text{Na}_2\text{Fe}_2(\text{SO}_4)_3$. Trace amount of $\text{Na}_6\text{Fe}(\text{SO}_4)_4$ (4.4 wt%) is also included in the analysis as an impurity. The Rietveld atomic

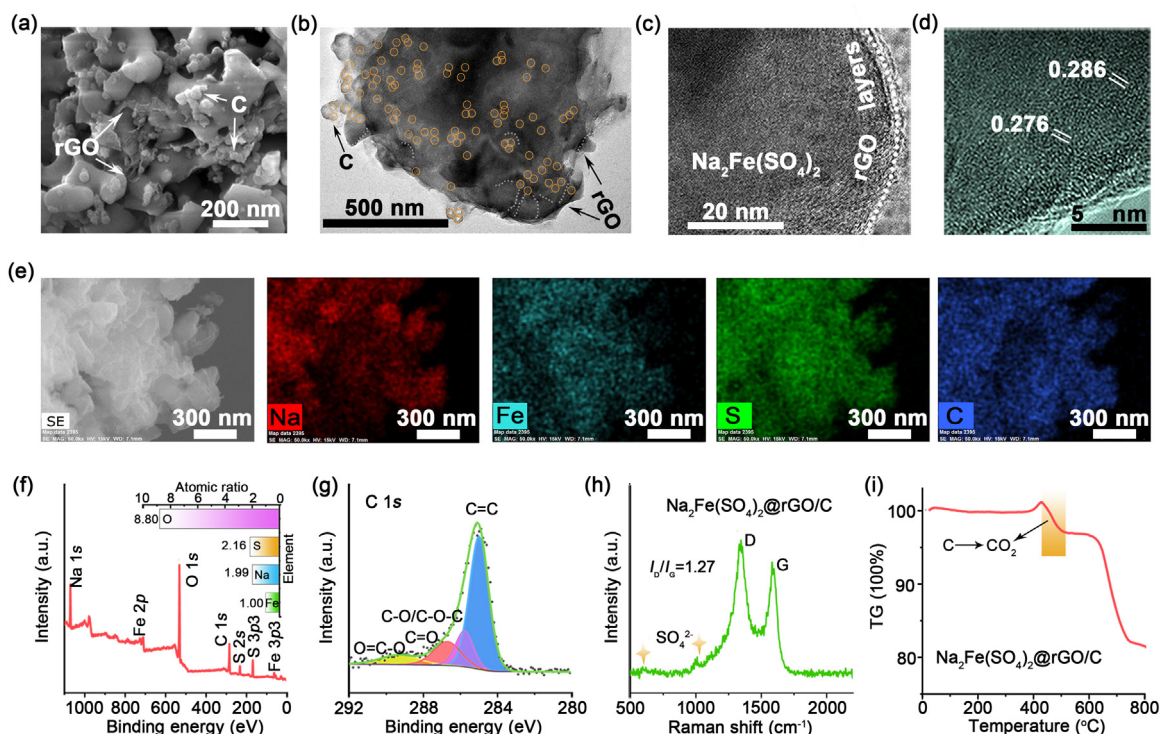
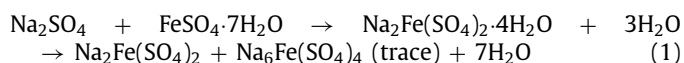


Fig. 2. Structural and morphological characterization of $\text{Na}_2\text{Fe}(\text{SO}_4)_2@\text{rGO}/\text{C}$. (a) SEM image. (b) TEM and (c) HRTEM images, illustrating the well combined hierarchical structure. (d) HRTEM image of a high degree of crystallinity. (e) The corresponding elements EDS mapping images of Na (red), Fe (cyan), S (green) and C (blue). (f) XPS spectrum and the contents ratio of elements (inset), further confirming the crystal phase of $\text{Na}_2\text{Fe}(\text{SO}_4)_2$. (g) High-resolution XPS spectrum of C 1 s. (h) Raman spectrum indicating the favorable conductivity of carbon matrix with I_D/I_G ratio of 1.13, and (i) TGA curve showing the low carbon content of 4.12 wt%.

parameters of $\text{Na}_2\text{Fe}(\text{SO}_4)_2@\text{rGO}/\text{C}$ based on the XRD data were shown in Table S2. Combined with the latter XPS (Fig. 2f) analysis, the main crystal phase was confirmed to be $\text{Na}_2\text{Fe}(\text{SO}_4)_2@\text{rGO}/\text{C}$. The typical peaks of carbon dots and rGO are not observed, perhaps due to their low contents in the composites. In contrast, the obtained $\text{Na}_2\text{Fe}(\text{SO}_4)_2$ without introducing carbon dots and rGO has poor crystallinity and contains higher contents of impurities: $\text{Na}_6\text{Fe}(\text{SO}_4)_4$, $\text{Fe}_2(\text{SO}_4)_3$ and Fe_2O_3 , as shown in Fig. S1(b). Therefore, the introduction of carbon dots and rGO is beneficial to phase purity and crystallinity of $\text{Na}_2\text{Fe}(\text{SO}_4)_2$, which could be explained by two aspects. First, carbon materials provide a local micro reductive environment during calcination to inhibit the oxidation of Fe^{2+} and reduce impurities. Second, inherent defects and oxygen-containing functional groups of GO could serve as crystal seeds to promote crystal growth and increase crystallinity [33,34]. The crystal structure of $\text{Na}_2\text{Fe}(\text{SO}_4)_2@\text{rGO}/\text{C}$ was shown in Fig. 1(c). The edge-sharing Fe_2O_{10} dimers are in turn linked by SO_4 tetrahedra with corner-sharing, forming a three-dimensional structure along the c-axis and a fast pathway for the diffusion of sodium ions located at the Na(2) and Na(3) sites. And the sodium ions at the Na(1) and SO_4 tetrahedra are arranged alternately. Based on the above analysis, the synthetic mechanism of sodium ferrous sulfate could be presented as following:



The morphology structure of as-synthesized $\text{Na}_2\text{Fe}(\text{SO}_4)_2@\text{rGO}/\text{C}$ was confirmed by scanning electron microscopy (SEM) and transmission electron microscope (TEM) images in Fig. 2(a–d). Typical SEM images of the $\text{Na}_2\text{Fe}(\text{SO}_4)_2@\text{rGO}/\text{C}$ (Figs. 2a and S2a) show that the nanoscale $\text{Na}_2\text{Fe}(\text{SO}_4)_2$ particles are uniformly distributed with large holes and interconnected via a little amount of rGO sheets. The carbon dots with diameter of 40 nm effectively

distribute the whole space to strengthen the connection between active materials and carbon matrix. TEM images (Fig. 2b) further display the cross-linked and hierarchical structure with rGO and carbon dots homogeneously distributing around $\text{Na}_2\text{Fe}(\text{SO}_4)_2$ particles, while Fig. 2(c) reveals the well connected thin rGO layers and active materials. Therefore, a continuous and hierarchical cross-linked structure was formed with slight rGO sheets ensuring the fast electron/ion transfer like a porous current collector, while carbon dots further promoted the conductivity. Moreover, the small particle sizes of $\text{Na}_2\text{Fe}(\text{SO}_4)_2$ would shorten the Na^+ transport distance. High-resolution TEM image (Fig. 2d) displays the lattice fringes of $\text{Na}_2\text{Fe}(\text{SO}_4)_2@\text{rGO}/\text{C}$ composites, 0.286 and 0.311 Å, matching with diffraction peaks of $2\theta = 31.26^\circ$ (400) and 28.63° (11–2) in XRD, respectively. The above results indicate the successful synthesis of the hierarchical porous $\text{Na}_2\text{Fe}(\text{SO}_4)_2@\text{rGO}/\text{C}$ composites with highly cross-linked structure. While the sample $\text{Na}_2\text{Fe}(\text{SO}_4)_2$ aggregated seriously with a large particle size of 1–2 μm , as shown in Fig. S2(b). Consequently, the introducing of carbon materials held the key to the nanosize and evenly distribution of $\text{Na}_2\text{Fe}(\text{SO}_4)_2@\text{rGO}/\text{C}$ composite with inhibiting the growth of crystal grains and preventing aggregation [35–37], with Fig. S3 giving more direct evidence. The energy dispersive spectroscopy (EDS) mapping in Fig. 2(e) confirms that the elements Na (red), Fe (cyan), S (green) and C (blue) are similarly homogeneously distributed in $\text{Na}_2\text{Fe}(\text{SO}_4)_2@\text{rGO}/\text{C}$, indicating their successful tight combination.

Nitrogen isothermal adsorption-desorption analyses were carried out to reveal the Brunauer-Emmett-Teller (BET) specific surface areas of the samples. The BET specific area of the as-synthesized $\text{Na}_2\text{Fe}(\text{SO}_4)_2@\text{rGO}/\text{C}$ is measured as $15.23 \text{ m}^2 \text{ g}^{-1}$ (Fig. S4a). The pore-size distribution curve (Fig. S4b) indicates the pore size is average 9.1389 nm. The low specific surface area is beneficial for the higher initial coulombic efficiency due to the less electrolyte decomposition, while the pore structure could contribute to the fast ion transfer. XPS spectrum of

$\text{Na}_2\text{Fe}(\text{SO}_4)_2/\text{rGO}/\text{C}$ composite powder was collected to gain insight into the chemical configurations. The survey spectrum (Fig. 2f) presented the signals associated with Na, Fe, S, O and C. The atomic ratio of Na/Fe/S/O was acquired from the fitted peak area of relevant elements with semi-quantitative analysis, giving ratios of 1.99: 1: 2.16: 8.8, indicating the major crystalline phase of $\text{Na}_2\text{Fe}(\text{SO}_4)_2$ with relatively higher purity. In high resolution C 1 s spectrum of $\text{Na}_2\text{Fe}(\text{SO}_4)_2/\text{rGO}/\text{C}$ composite, in Fig. 2(g), four fitted peaks centered at 284.6, 285.4, 286.3 and 288.96 eV refer to C–C/C=C, C–O/C–O–C, C=O and O–C=O bonds [38,39], respectively, indicating the partial reduction of GO owing to the low annealing temperature. The FT-IR spectrum displays the typical features of SO_4^{2-} group in Fig. S5, in which the signals located at 1082, 992 and 626 cm^{-1} are assigned to asymmetric vibration, symmetric stretching, and asymmetric bending of SO_4^{2-} group, respectively [40]. Additionally, the broad band located at $\approx 3200 \text{ cm}^{-1}$ is induced from symmetric/asymmetric stretching of OH^- in rGO, confirming its existence in nanocomposites. In Raman spectroscopy (Fig. 2h), the peaks located at 600 and 1004 cm^{-1} are attributed to the ν_1 and ν_2 stretching vibrations of SO_4^{2-} respectively [30], proving the high crystallinity of the host $\text{Na}_2\text{Fe}(\text{SO}_4)_2$ in the nano-composite. In addition, the two prominent signatures located at around 1342 and 1583 cm^{-1} are discerned to the D-band (defects and disorders in the carbon layer) and G-band (ordered structure of sp^2 carbon atoms in plane) deriving from the carbon [41,42], respectively. Clearly, $\text{Na}_2\text{Fe}(\text{SO}_4)_2/\text{rGO}/\text{C}$ performed I_D/I_G ratio of 1.13, indicating desirable reduction of graphene oxide enabling the favorable conductivity of carbon matrix. The carbon content in the $\text{Na}_2\text{Fe}(\text{SO}_4)_2/\text{rGO}/\text{C}$ composite was calculated to be 4.12 wt% by thermogravimetric analysis (TGA) in the air (Fig. 2i), which is lower than the reported Fe-based sulfates materials, favorable for the high energy density of the whole material.

The electrochemical properties of $\text{Na}_2\text{Fe}(\text{SO}_4)_2/\text{rGO}/\text{C}$ nanocomposites were investigated in assembled Na-ion half cells at room temperature. In cyclic voltammograms (CV) test of $\text{Na}_2\text{Fe}(\text{SO}_4)_2/\text{rGO}/\text{C}$ (Fig. 3a), peaks located at 3.64/3.34, 3.9/3.63 V and 4.12/3.94 V are related to the reversible de/intercalation of Na^+ , including the $\text{Fe}^{2+}/\text{Fe}^{3+}$ couple transformation as discussed by later XPS study. A pair of weak peaks at 3.03/2.85 V may be caused by trace impurities, and peak at 4.49 V is associated with side effects, which would result in partially irreversible capacity, similar to the reported works. The curves of the first cycle are different from the latter's, which is related to the partially irreversible structural transformation during first desodiation process, as indicated in the previous report [43]. Besides, it was also relevant to the formation of the cathode electrolyte interface (CEI) layer, due to the irreversible decomposition of little amount of electrolyte during the charging and discharging process. Thus, the initial coulombic efficiency in this work was 84.7%, lower than 100%, similar to the reported alluaudite-type Fe-based sulfates materials in sodium ion battery (Table S3). Surprisingly, the voltage-energy density profiles in initial three cycles at 0.05 C in Fig. 3(b) show that $\text{Na}_2\text{Fe}(\text{SO}_4)_2/\text{rGO}/\text{C}$ exhibits a brief voltage platform at around 3.75 V, in accordance with the calculated values in the literature [44], and higher than the reported experimental result of $\text{Na}_2\text{Fe}(\text{SO}_4)_2$ [31]. Moreover, it achieves specific capacity of 85 mAh g^{-1} and high energy density of 330 Wh kg^{-1} in the first cycle. More importantly, the curves of the $\text{Na}_2\text{Fe}(\text{SO}_4)_2/\text{rGO}/\text{C}$ electrode show better symmetry, indicating smaller polarization, which is associated with the highly conductive hierarchical architecture. In addition, the energy density of $\text{Na}_2\text{Fe}(\text{SO}_4)_2/\text{rGO}/\text{C}$ has no decline in the initial three cycles, suggesting the high reversibility.

The excellent rate performances of $\text{Na}_2\text{Fe}(\text{SO}_4)_2/\text{rGO}/\text{C}$ electrodes were presented in Fig. 3(c), with reversible capacities of 85, 78, 72, 62, 58, 50, 40 and 22 mAh g^{-1} at various C-rates of 0.05, 0.1, 0.2, 0.5, 1, 2, 5 and 10 C, respectively. When the cur-

rent density backed to 0.1 C, the reversible capacity recovered to 79 mAh g^{-1} , exhibiting a strong tolerance for the fast and reversible Na^+ insertion/extraction. More importantly, the midpoint voltage of $\text{Na}_2\text{Fe}(\text{SO}_4)_2/\text{rGO}/\text{C}$ exhibits quite good stability at different rates, indicating its relatively weak polarization at higher current densities. The typical charge-discharge curves at different rates in Fig. 3(d) further confirm the excellent Na^+ storage properties of $\text{Na}_2\text{Fe}(\text{SO}_4)_2/\text{rGO}/\text{C}$ composite. In addition, the $\text{Na}_2\text{Fe}(\text{SO}_4)_2/\text{rGO}/\text{C}$ electrode delivers an initial discharge capacity of 72 mAh g^{-1} with initial coulombic efficiency of 95.6% at 0.2 C, and capacity retention rate reaches 89.6% after 100 cycles. The corresponding charge/discharge curves at different cycles in Fig. 3(f), also demonstrate the outstanding reversibility and stability. More importantly, the midpoint voltage of $\text{Na}_2\text{Fe}(\text{SO}_4)_2/\text{rGO}/\text{C}$ electrode at 0.5 C displays no observable decay over 200 cycles in Fig. 3(g), with a high capacity retention of 81.2% over 200 cycles and approximately 100% coulombic efficiencies (Fig. S6b), indicating a negligible polarization and long cycle stability, better than the reported limited 50 cycles at 0.1 C of $\text{Na}_2\text{Fe}(\text{SO}_4)_2$ [31]. In addition, several types of Fe-based cathode materials in SIBs were compared with operating voltage in Fig. 3(h). It can be seen that as-prepared $\text{Na}_2\text{Fe}(\text{SO}_4)_2/\text{rGO}/\text{C}$ has a relatively high voltage (3.75 V vs. Na^+/Na) [25,45–51], benefiting the high energy density. The superior performance of $\text{Na}_2\text{Fe}(\text{SO}_4)_2/\text{rGO}/\text{C}$ composite is attributed to the novel hierarchical nanostructure with slight rGO sheets working as current collector sufficiently enhancing electron transfer and offering smooth ion channels, while, the carbon dots' assistance further promoting the conductivity of whole architecture.

The success of $\text{Na}_2\text{Fe}(\text{SO}_4)_2/\text{rGO}/\text{C}$ in sodium-ion half batteries strongly encourages us to demonstrate their practical application in sodium-ion full batteries. The hard carbon/rGO composite (HC/G) was employed as anode to match with $\text{Na}_2\text{Fe}(\text{SO}_4)_2/\text{rGO}/\text{C}$ cathode, and the full cell is assigned as HC/G// $\text{Na}_2\text{Fe}(\text{SO}_4)_2/\text{rGO}/\text{C}$. The sodium storage properties of the anode in the half cell are provided in Fig. S7, delivering a reversible capacity of about 175 mAh g^{-1} at 100 mA g^{-1} and stable cycling for 80 cycles in the voltage range of 0.01–3.0 V. In order to obtain a better electrochemical performance in the full cell, the anode was pre-activated to form a stable SEI. The capacity ratio of anode to cathode is approximately 1:1.5 to ensure that cathode material is fully utilized. The typical galvanostatic charge-discharge curves of the cathode $\text{Na}_2\text{Fe}(\text{SO}_4)_2/\text{rGO}/\text{C}$ and anode HC/G were shown in Fig. 3(i). The charge-discharge profiles of the full cell HC/G// $\text{Na}_2\text{Fe}(\text{SO}_4)_2/\text{rGO}/\text{C}$ (Fig. 3j) show a high capacity of 67 mAh g^{-1} , 196.67 Wh kg^{-1} at 0.1 C (calculated based on the mass of cathode) with the high midpoint voltage of about 3.0 V, and the cycling performance at 0.1 C is shown in Fig. S8. Impressively, it could continuously light up six Light-Emitting Diodes (LEDs) in Fig. S9, suggesting great practicability in actual application. Most importantly, the HC/G// $\text{Na}_2\text{Fe}(\text{SO}_4)_2/\text{rGO}/\text{C}$ full cell is competitive compared with recently reported sodium ion full cells concerning their midpoint voltage [52–63], as presented in Fig. 3(k). According to the above results, hierarchical porous $\text{Na}_2\text{Fe}(\text{SO}_4)_2/\text{rGO}/\text{C}$ nano-composite with robust cross-linked carbon matrix with high conductivity is a promising SIBs cathode material for energy storage equipment.

The kinetic analysis based on CV curves was also carried out to further understand the good electrochemical performance of $\text{Na}_2\text{Fe}(\text{SO}_4)_2/\text{rGO}/\text{C}$. The CV curves at various scan rates from 0.1 to 0.4 mV s^{-1} (Fig. 4a) display similar shapes, proving that the electrochemical reaction has good reversibility with the increasing scan rates. According to the relationship between the measured current (i) and the scan rate (ν) [64]:

$$i = a\nu^b \quad (2)$$

the b value can be determined by the slope of $\log(\nu)$ - $\log(i)$ plots. In special, when the b value equals 0.5, electrochemical process

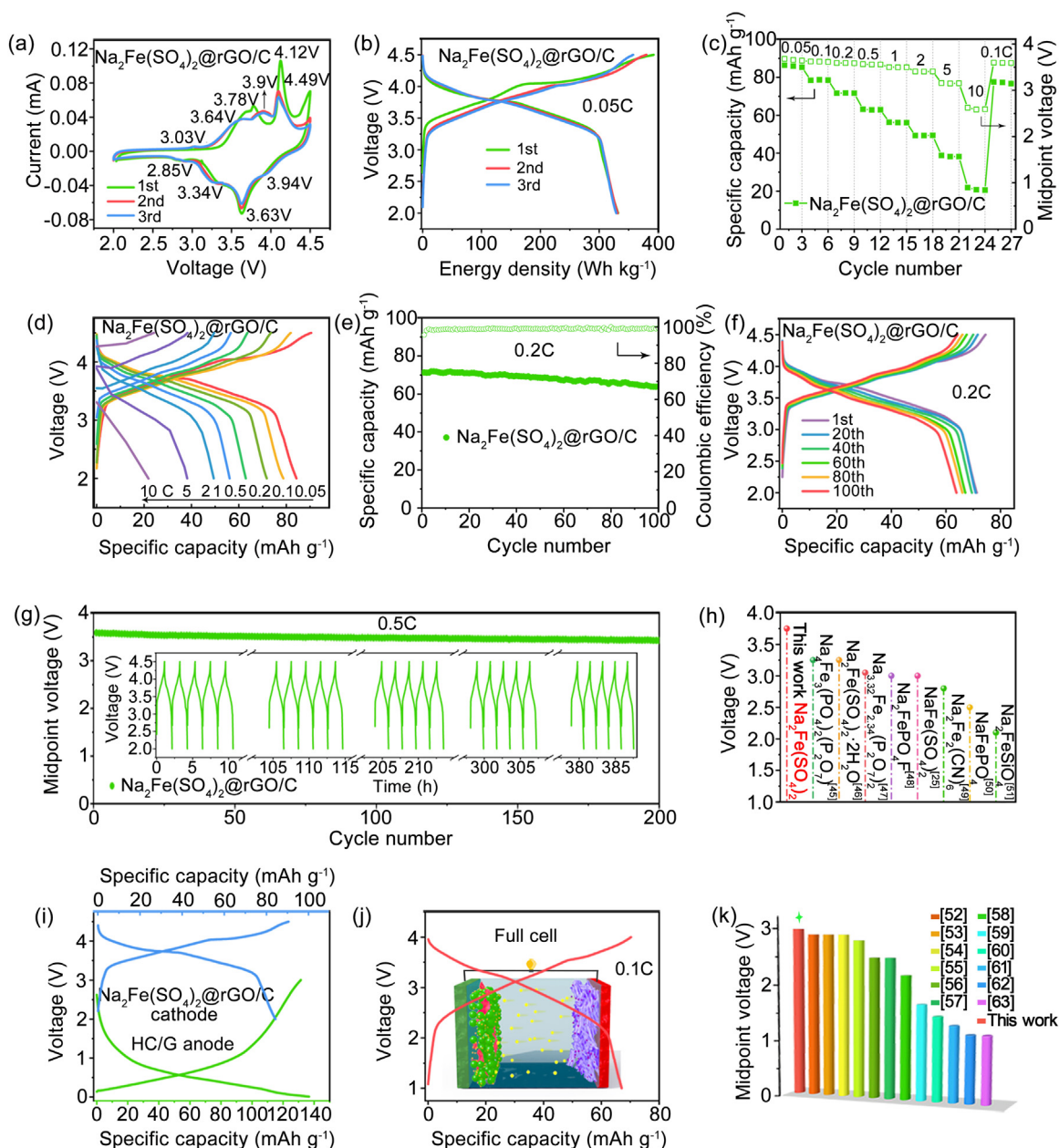


Fig. 3. Sodium storage performance of $\text{Na}_2\text{Fe}(\text{SO}_4)_2@\text{rGO}/\text{C}$ as cathode for sodium-ion half-cell and full-cell. (a) CV profiles at a scan rate of 0.1 mV s^{-1} . (b) Voltage-energy density profiles at 0.05 C rate ($1 \text{ C} = 91.15 \text{ mAh g}^{-1}$) for initial three cycles. (c) Rate capability at different rates. (d) Corresponding charge/discharge profiles at different C-rates. (e) Cycle performance at 0.2 C rate and its (f) Representative charge/discharge curves with different cycles. (g) Long-term cycling performances of midpoint voltage at 0.5 C (insert: Voltage-time profiles for special cycles). (h) Comparison of operating voltage with different iron-based cathode materials in SIBs. (i) Galvanostatic curves of $\text{Na}_2\text{Fe}(\text{SO}_4)_2@\text{rGO}/\text{C}$ cathode (blue) and HC/G anode (green). (j) Charge-discharge profiles of the HC/G// $\text{Na}_2\text{Fe}(\text{SO}_4)_2@\text{rGO}/\text{C}$ full cell and schematic illustration of sodium ion full cell (inset). (k) Comparison between this work and other literature works on sodium-ion full cells in the aspects of midpoint voltage.

is a total diffusion-controlled behavior, whereas a b value of 1.0 represents a surface controlled behavior [65]. Clearly, in Fig. 4(b), the b values of peak group 1–3 are 0.64, 0.95 and 0.85, respectively, which demonstrates the dominated surface controlled reaction process. Based on the equation: $i = k_1 v + k_2 v^{-1/2}$, the quantitative surface-controlled capacity contribution could be acquired. Fig. 4(c) detailedly illustrates the contribution of surface-controlled capacity at 0.3 mV s^{-1} and was calculated to be 69% with orange area. The quantified results (Fig. 4d) show that the surface-controlled capacity rises gradually with increasing the scan rate, and reaches 74% at 0.4 mV s^{-1} , indicating that surface

controlled behavior dominates Na^+ storage process at high scan rate and is beneficial for obtaining superior high rate performance.

Additionally, EIS plots were employed to study reaction kinetics of the electrodes and the equivalent electrical circuit was fitted in Fig. 4(e). The values of physical elements of R_1 (electrolyte impedance), CPE (constant phase element), R_2 (charge transfer impedance related to faraday process) and W_0 (Warburg impedance) are displayed in Table S5 [66,67]. Attractively, the results show that $\text{Na}_2\text{Fe}(\text{SO}_4)_2@\text{rGO}/\text{C}$ electrode has a lower R_2 (320.3Ω) value, revealing the elevated kinetics in charge transfer process. Moreover, the Na^+ diffusion coefficient (D_{Na^+}) was

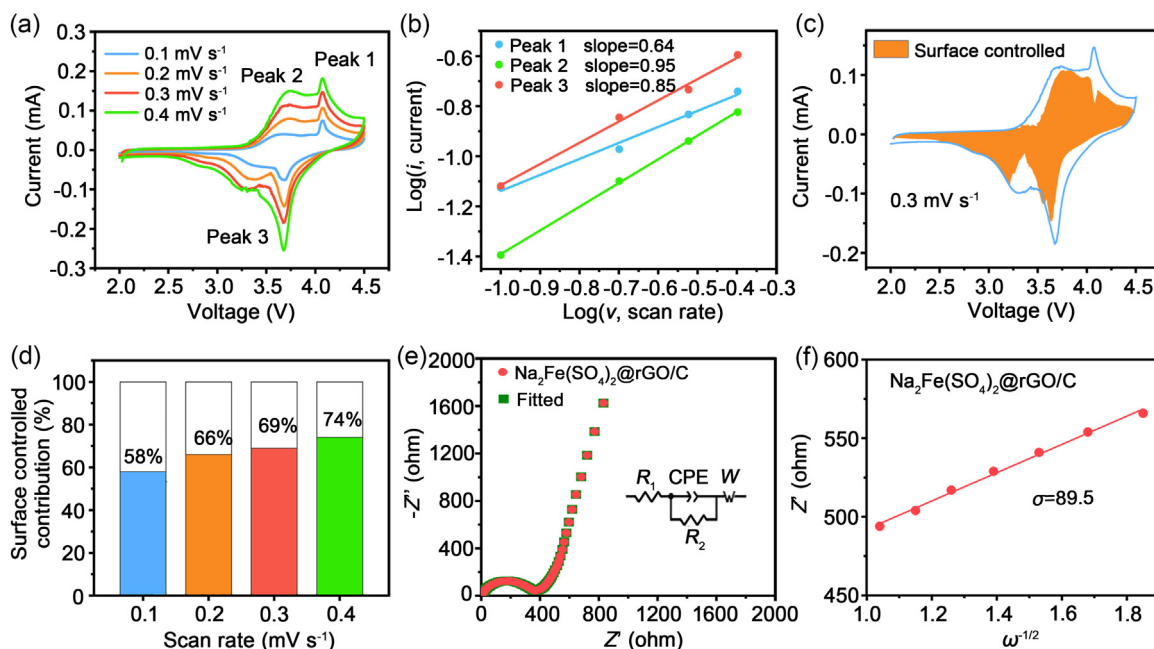


Fig. 4. Kinetic analysis of sodium-storage behavior of $\text{Na}_2\text{Fe}(\text{SO}_4)_2@\text{rGO}/\text{C}$: (a) CV curves at different scan rates. (b) $\text{Log}(i)$ vs. $\text{log}(v)$ plot. (c) The surface controlled capacity contribution (orange area) at 0.3 mV s^{-1} . (d) Contribution ratio of surface controlled capacity at various scan rates. (e) EIS plots of $\text{Na}_2\text{Fe}(\text{SO}_4)_2@\text{rGO}/\text{C}$ electrodes (inset: corresponding fitted equivalent circuit model). (f) Corresponding linear fitting of Z' vs. $\omega^{-1/2}$ plots in the low-frequency range of $\text{Na}_2\text{Fe}(\text{SO}_4)_2@\text{rGO}/\text{C}$ electrodes.

calculated based on the Eq. (3):

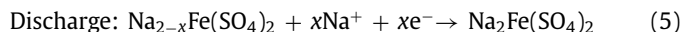
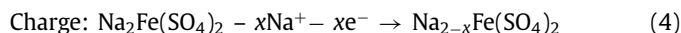
$$D_{\text{Na}^+} = \frac{R^2 T^2}{2A^2 n^4 F^4 C^2 \sigma^2} \quad (3)$$

where R , T , A , n , F , C and σ represent gas constant, temperature, surface area, the number of electrons transferred in the reaction process, Faraday constant, concentration of Na^+ and Warburg constant, respectively. The σ equals the slope of Z' versus $\omega^{-1/2}$ in the low-frequency region [68,69], displayed in Fig. 4(f). The calculated D_{Na^+} of $\text{Na}_2\text{Fe}(\text{SO}_4)_2@\text{rGO}/\text{C}$ electrode is $1.19 \times 10^{-12} \text{ cm}^2 \text{ s}^{-1}$, demonstrating fast Na^+ diffusion. The lower R_2 and higher D_{Na^+} responsibly interpret the fast kinetics and, therefore, superior sodium storage performance of $\text{Na}_2\text{Fe}(\text{SO}_4)_2@\text{rGO}/\text{C}$ electrode achieved by the robust cross-linked hierarchical structure with multilevel carbon matrix remarkably boosted the ion/electron transfer.

In order to clarify the sodium storage mechanism, the ex-situ XRD and XPS were employed to characterize the $\text{Na}_2\text{Fe}(\text{SO}_4)_2@\text{rGO}/\text{C}$ electrodes at different states. When charged to 4.5 V, typical characteristic peaks at 13.8° , 15.5° , 28.63° , 30.0° , 31.26° and 32.0° , corresponding to (020), (200), (11–2), (31–2), (400) and (240), respectively, shifted slightly towards the lower angle (Fig. 5a), similar with the reported result [16]. This lattice space expansion may be due to the change of the internal electrostatic force in the lattice caused by the desodiation. In addition, the diffraction peaks of 31.2° (400) and 32.0° (240) became weaker obviously, and this could be ascribed to sodium ion migration along the c axis for both the Na(2) and Na(3) sites [70]. When discharged to 2.0 V, all diffraction peaks returned to the original state and the peak at 31.2° (400) reappear. These indicate successfully reversible lattice breathing and crystal phase transformation during operation. The reaction mechanism was further analyzed with ex-situ XPS concerning the redox reaction of $\text{Fe}^{2+}/\text{Fe}^{3+}$ (Fig. 5b). In the pristine state, Fe^{2+} (peaking at 711.2 and 724.6 eV) was dominated with less Fe^{3+} (peaking at 715 and 730 eV) [71,72], which may be associated with the slight surface oxidation of $\text{Na}_2\text{Fe}(\text{SO}_4)_2@\text{rGO}/\text{C}$. When charged to 4.5 V, the main peak of Fe^{3+} (715 eV) strengthened and the peaks of Fe^{2+} decayed, suggesting the main conversion of Fe^{2+} to Fe^{3+} , relevant to the

extraction of Na^+ . And the incomplete valence state transformation was consistent with the insufficient sodiation, corresponding to the capacity, that below the theoretical specific capacity, in initial charge process. While discharged to 2.0 V, Fe 2p spectrum returned back similar to the initial state. The pie charts in Fig. 5(b) also present the fitted peak area ratios of Fe^{2+} and Fe^{3+} at three different states, and Fig. 5(c) exhibits the ratio of sodium to iron and sulfur, all revealing good reversibility of the redox reaction.

The favorable recovered crystal phase along with the excellent electrochemical performance strongly evidences the advanced architecture design of $\text{Na}_2\text{Fe}(\text{SO}_4)_2@\text{rGO}/\text{C}$ cathode. The exquisite hierarchical structure provides the high-speed ion/electron transfer routes as well as the robust skeleton, allowing the simultaneous achievement of fast kinetics and durable elastic structure. And based on the above analysis, it could be seen as a solid-solution transition process during sodiation/desodiation, and the main phase reaction equation is described as follows:



Surface chemistry investigation of $\text{Na}_2\text{Fe}(\text{SO}_4)_2@\text{rGO}/\text{C}$ electrode was also conducted by XPS, and the element content information of three states were displayed in Fig. 5(d) and Table S6. As the charging voltage rises, the content of C and F element show obvious increasing, corresponding to the formation of cathode electrolyte interface (CEI) layer. It is also evidenced that the decreasing of element content of bulk materials because of the shielding effect of passivation layer, such as Na, Fe, S and O element. The increasing of F content during the whole intercalation/deintercalation process indicates the CEI layer formed and gradually became complete. In addition, the constant increasing of CE to nearly 100% in the initial 5 cycles of $\text{Na}_2\text{Fe}(\text{SO}_4)_2@\text{rGO}/\text{C}$ also proves the gradual formation process (Table S4). For detailed composition of CEI film, the C 1s, Na 1s and O 1s spectra at pristine, charged to 4.5 V and discharged to 2.0 V were further analyzed in Fig. 5(e). In C 1s spectra, the C–F peak [73] (~290.7 eV) emerged

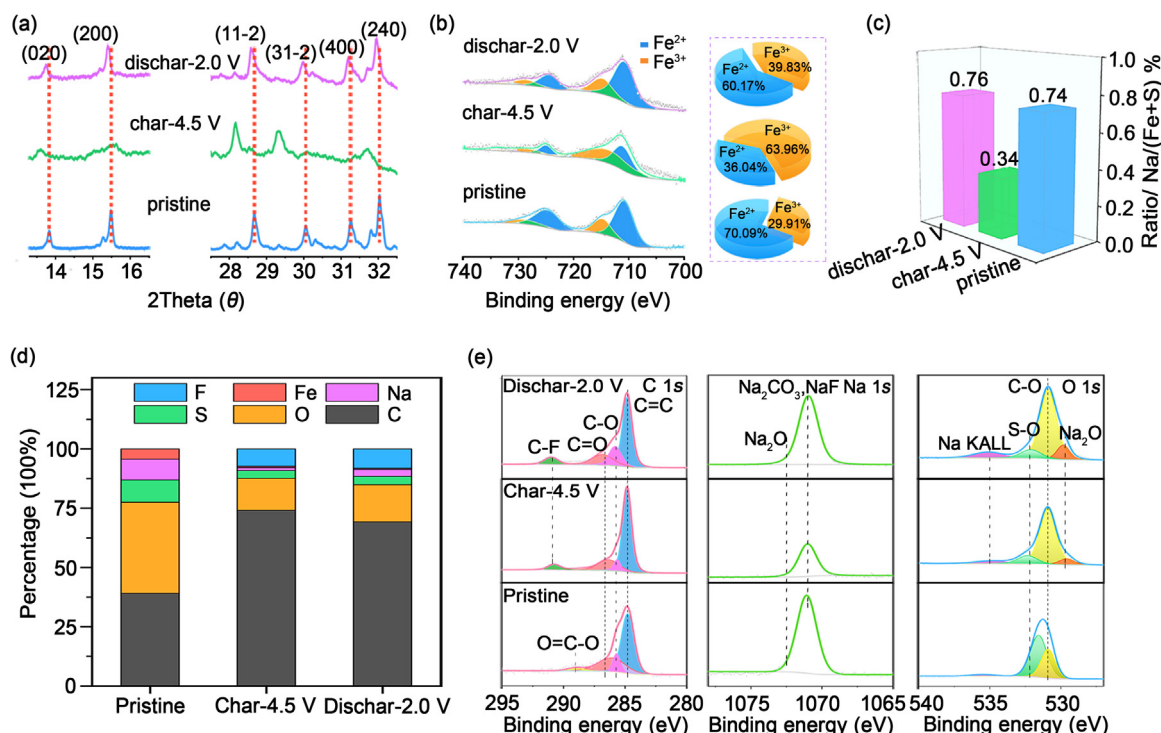


Fig. 5. Sodium storage mechanism and surface chemistry investigation of $\text{Na}_2\text{Fe}(\text{SO}_4)_2@\text{rGO}/\text{C}$ electrode. (a) Ex-situ XRD patterns at different charged/discharged states. (b) XPS spectra of Fe 2p and ratios of Fe^{2+} and Fe^{3+} . (c) Ratios of sodium to iron and sulfur of $\text{Na}_2\text{Fe}(\text{SO}_4)_2@\text{rGO}/\text{C}$ electrode at states of pristine, first charged to 4.5 V and discharged to 2.0 V. (d) Element content information. (e) High resolution XPS spectra of C 1s, Na 1s and O 1s.

with initial desodiation process, and the peak area increases with the further sodiation reaction. In addition, the peaks areas of C=C (284.6 eV), C–O (285.4 eV) and C=O (286.3 eV) are bigger than the pristine, indicating the formation of CEI layer. Na_2CO_3 and Na–F (~ 1071.5 eV) and Na_2O (~ 1072.5 eV) [74] appeared in the Na 1s spectra after charged and discharged, which are related to the decomposition of electrolytes. Na_2O peaks are also observed at O 1s peaks in the charged electrodes, and strengthened after discharging. The above results evidence the formation of CEI film on electrode surface in initial charge process and its completion with further discharging, based on the typical peaks' strength. This gradual improvement property of CEI could contribute to the stable surface chemistry of electrode and promote the structural and chemical durability of active materials, therefore, benefiting for the advanced sodium storage performance [75].

3. Conclusions

In summary, a high-voltage, $\text{Na}_2\text{Fe}(\text{SO}_4)_2@\text{rGO}/\text{C}$ nano-composite, was rationally designed and facilely prepared via a simple low-temperature synthesis method and cheap raw materials as cathode for SIBs. With low carbon content of 4.12 wt%, the multi-level carbon matrix functioned as cross-linked conductive skeleton to provide fast ion/electron transport channels to highly boost the reaction kinetics of $\text{Na}_2\text{Fe}(\text{SO}_4)_2$. Therefore, the $\text{Na}_2\text{Fe}(\text{SO}_4)_2@\text{rGO}/\text{C}$ nano-composite exhibits fascinating sodium storage performance. It achieves high energy density of 330 Wh kg^{-1} (85 mAh g^{-1}) at 0.05 C with high voltage platform about 3.75 V, superior rate performance (58 mAh g^{-1} at 1 C, 5805 W kg^{-1} at 10 C), and excellent cycling stability (200 cycles at 0.5 C with 81.2% retention). Meanwhile, ex-situ XRD and XPS analysis strongly confirm the high reversible sodiation/desodiation process, and the gradual improvement property of surface chemistry of electrode. More significantly, the assembled full cell delivers a high midpoint voltage of 3 V and high capacity of 67 mAh g^{-1}

(196.67 Wh kg^{-1}) at 0.1 C (calculated based mass of active material in cathode). This work provides a high voltage, low-cost cathode for SIBs as well as novel architecture design, which could be extended as a rational strategy for various low-conductive electrodes.

Declaration of Competing Interest

The authors declare that they have no known competing financial interests or personal relationships that could have appeared to influence the work reported in this paper.

Acknowledgments

This work was supported by the National Natural Science Foundation of China (Nos. 21771164, U1804129 and 21671205), Postdoctoral Research Grant in Henan Province (001702055), Center of Advanced Analysis & Gene Sequencing of Zhengzhou University and the Zhongyuan Youth Talent support program in Henan province.

Supplementary materials

Supplementary material associated with this article can be found, in the online version, at doi:10.1016/j.jchem.2020.03.047.

References

- [1] Q. Li, Z. Liu, F. Zheng, R. Liu, J. Lee, G.L. Xu, G. Zhong, X. Hou, R. Fu, Z. Chen, K. Amine, J. Mi, S. Wu, C.P. Grey, Y. Yang, *Angew. Chem. Int. Ed.* 57 (2018) 11918–11923.
- [2] K. Song, C. Liu, L. Mi, S. Chou, W. Chen, C. Shen, *Small* (2019) 1903194, doi:10.1002/sml.201903194.
- [3] Y. Huang, M. Xie, J. Zhang, Z. Wang, Y. Jiang, G. Xiao, S. Li, L. Li, F. Wu, R. Chen, *Nano Energy* 39 (2017) 273–283.
- [4] J. Deng, W.-B. Luo, S.-L. Chou, H.-K. Liu, S.-X. Dou, *Adv. Energy Mater.* 8 (2018) 1701428.
- [5] Y. Fang, Q. Liu, L. Xiao, Y. Rong, Y. Liu, Z. Chen, X. Ai, Y. Cao, H. Yang, J. Xie, C. Sun, X. Zhang, B. Aoun, X. Xing, X. Xiao, Y. Ren, *Chem* 4 (2018) 1167–1180.

- [6] Y. Wang, Y. Wang, Y.-X. Wang, X. Feng, W. Chen, X. Ai, H. Yang, Y. Cao, *Chem* 5 (2019) 2547–2570.
- [7] M. Chen, W. Hua, J. Xiao, D. Cortie, X. Guo, E. Wang, Q. Gu, Z. Hu, S. Indris, X.L. Wang, S.L. Chou, S.X. Dou, *Angew. Chem. Int. Ed.* 59 (2020) 2449–2456.
- [8] Y. Liu, Q. Shen, X. Zhao, J. Zhang, X. Liu, T. Wang, N. Zhang, L. Jiao, J. Chen, L.Z. Fan, *Adv. Funct. Mater.* 30 (2019) 1907837.
- [9] C. Zhao, Z. Yao, J. Wang, Y. Lu, X. Bai, A. Aspuru-Guzik, L. Chen, Y.-S. Hu, *Chem* 5 (2019) 2913–2925.
- [10] C. Zhao, F. Ding, Y. Lu, L. Chen, Y.S. Hu, *Angew. Chem. Int. Ed.* 59 (2020) 264–269.
- [11] Y. Xiao, P.-F. Wang, Y.-X. Yin, Y.-F. Zhu, X. Yang, X.-D. Zhang, Y. Wang, X.-D. Guo, B.-H. Zhong, Y.-G. Guo, *Adv. Energy Mater.* 8 (2018) 1800492.
- [12] L. Liang, X. Sun, D.K. Denis, J. Zhang, L. Hou, Y. Liu, C. Yuan, *ACS Appl. Mater. Interfaces* 11 (2019) 4037–4046.
- [13] J. Qian, C. Wu, Y. Cao, Z. Ma, Y. Huang, X. Ai, H. Yang, *Adv. Energy Mater.* 8 (2018) 1702619.
- [14] W.-J. Li, S.-L. Chou, J.-Z. Wang, Y.-M. Kang, J.-L. Wang, Y. Liu, Q.-F. Gu, H.-K. Liu, S.-X. Dou, *Chem. Mater.* 27 (2015) 1997–2003.
- [15] J. Xu, J. Chen, S. Zhou, C. Han, M. Xu, N. Zhao, C.-P. Wong, *Nano Energy* 50 (2018) 323–330.
- [16] J. Cao, Y. Wang, L. Wang, F. Yu, J. Ma, *Nano Lett.* 19 (2019) 823–828.
- [17] F. Xiong, Q. An, L. Xia, Y. Zhao, L. Mai, H. Tao, Y. Yue, *Nano Energy* 57 (2019) 608–615.
- [18] G. Yan, S. Mariyappan, G. Rousse, Q. Jacquet, M. Deschamps, R. David, B. Mirvaux, J.W. Freeland, J.-M. Tarascon, *Nat. Commun.* 10 (2019) 585.
- [19] Y. Meng, T. Yu, S. Zhang, C. Deng, *J. Mater. Chem. A* 4 (2016) 1624–1631.
- [20] P. Barpanda, *Israel J. Chem.* 55 (2015) 537–557.
- [21] H.J. Song, D.-S. Kim, J.-C. Kim, S.-H. Hong, D.-W. Kim, *J. Mater. Chem. A* 5 (2017) 5502–5510.
- [22] X. Chen, K. Du, Y. Lai, G. Shang, H. Li, Z. Xiao, Y. Chen, J. Li, Z. Zhang, *J. Power Sources* 357 (2017) 164–172.
- [23] M. Reynaud, G. e. Rousse, A.M. Abakumov, M.T. Sougrati, G.V. Tendeloo, J.-N. e. Chotard, J.-M. Tarascon, *J. Mater. Chem. A* 2 (2014) 2671–2680.
- [24] Y. Meng, S. Zhang, C. Deng, *J. Mater. Chem. A* 3 (2015) 4484–4492.
- [25] P. Singh, K. Shiva, H. Celio, J.B. Goodenough, *Energy Environ. Sci.* 8 (2015) 3000–3005.
- [26] P. Barpanda, G. Oyama, S.-i. Nishimura, S.-C. Chung, A. Yamada, *Nat. Commun.* 5 (2014) 4358.
- [27] A. Gutierrez, N.A. Benedek, A. Manthiram, *Chem. Mater.* 25 (2013) 4010–4016.
- [28] J. Gao, X. Sha, X. Liu, L. Song, P. Zhao, *J. Mater. Chem. A* 4 (2016) 11870–11877.
- [29] T. Yu, B. Lin, Q. Li, X. Wang, W. Qu, S. Zhang, C. Deng, *Phys. Chem. Phys.* 18 (2016) 26933–26941.
- [30] Y. Liu, R. Rajagopalan, E. Wang, M. Chen, W. Hua, B. Zhong, Y. Zhong, Z. Wu, X. Guo, *ACS Sustain. Chem. Eng.* 6 (2018) 16105–16112.
- [31] W. Pan, W. Guan, S. Liu, B.B. Xu, C. Liang, H. Pan, M. Yana, Y. Jiang, *J. Mater. Chem. A* 7 (2019) 13197–13204.
- [32] X. Zhu, D. Liu, D. Zheng, G. Wang, X. Huang, J. Harris, D. Qu, D. Qu, *J. Mater. Chem. A* 6 (2018) 13294–13301.
- [33] X. Cao, A. Pan, S. Liu, J. Zhou, S. Li, G. Cao, J. Liu, S. Liang, *Adv. Energy Mater.* 7 (2017) 1700797.
- [34] K.S. Novoselov, V.I. Fal'ko, L. Colombo, P.R. Gellert, M.G. Schwab, K. Kim, *Nature* 490 (2012) 192–200.
- [35] H. Li, T. Jin, X. Chen, Y. Lai, Z. Zhang, W. Bao, L. Jiao, *Adv. Energy Mater.* 8 (2018) 1801418.
- [36] X. Xiang, Q. Lu, M. Han, J. Chen, *Chem. Commun.* 52 (2016) 3653–3656.
- [37] Y. Jiang, Z. Yang, W. Li, L. Zeng, F. Pan, M. Wang, X. Wei, G. Hu, L. Gu, Y. Yu, *Adv. Energy Mater.* 5 (2015) 1402104.
- [38] R. Rajagopalan, B. Chen, Z. Zhang, X.-L. Wu, Y. Du, Y. Huang, B. Li, Y. Zong, J. Wang, G.-H. Nam, M. Sindoro, S.X. Dou, H.K. Liu, H. Zhang, *Adv. Mater.* 29 (2017) 1605694.
- [39] M. Guo, J. Wang, H. Dou, G. Gao, S. Wang, J. Wang, Z. Xiao, G. Wu, X. Yang, Z.-F. Ma, *Nano Energy* 56 (2019) 502–511.
- [40] A. Go-ni, A. Iturrondobeitia, I.G. d. Muro, L. Lezama, T. Rojo, *J. Power Sources* 369 (2017) 95–102.
- [41] J. Liu, Y. Zhang, L. Zhang, F. Xie, A. Vasileff, S.-Z. Qiao, *Adv. Mater.* 31 (2019) 1901261.
- [42] C. Shen, H. Long, G. Wang, W. Lu, L. Shao, K. Xie, *J. Mater. Chem. A* 6 (2018) 6007–6014.
- [43] W. Wang, X. Liu, Q. Xu, H. Liu, Y.-G. Wang, Y. Xia, Y. Cao, X. Ai, *J. Mater. Chem. A* 6 (2018) 4354–4364.
- [44] T. Watcharatharapong, S. Chakraborty, R. Ahuja, *J. Mater. Chem. A* 7 (2019) 17446–17455.
- [45] M. Chen, W. Hua, J. Xiao, D. Cortie, W. Chen, E. Wang, Z. Hu, Q. Gu, X. Wang, S. Indris, S.L. Chou, S.X. Dou, *Nat. Commun.* 10 (2019) 1480.
- [46] P. Barpanda, G. Oyama, C.D. Ling, A. Yamada, *Chem. Mater.* 26 (2014) 1297–1299.
- [47] M. Chen, L. Chen, Z. Hu, Q. Liu, B. Zhang, Y. Hu, Q. Gu, J.L. Wang, L.Z. Wang, X. Guo, S.L. Chou, S.X. Dou, *Adv. Mater.* 29 (2017) 1605535.
- [48] W. Ko, J.-K. Yoo, H. Park, Y. Lee, H. Kim, Y. Oh, S.-T. Myung, J. Kim, *J. Power Sources* 432 (2019) 1–10.
- [49] Y. You, H.R. Yao, S. Xin, Y.X. Yin, T.T. Zuo, C.P. Yang, Y.G. Guo, Y. Cui, L.J. Wan, J.B. Goodenough, *Adv. Mater.* 28 (2016) 7243.
- [50] Y. Liu, N. Zhang, F. Wang, X. Liu, L. Jiao, L.-Z. Fan, *Adv. Funct. Mater.* 28 (2018) 1801917.
- [51] B. Ali, A. ur-Rehman, F. Ghafoor, M.I. Shahzad, S.K. Shah, S.M. Abbas, *J. Power Sources* 396 (2018) 467–475.
- [52] Y. Wang, N. Xiao, Z. Wang, H. Li, M. Yu, Y. Tang, M. Hao, C. Liu, Y. Zhou, J. Qiu, *Chem. Eng. J.* 342 (2018) 52–60.
- [53] Y. Xiao, P.-F. Wang, Y.-X. Yin, Y.-F. Zhu, Y.-B. Niu, X.-D. Zhang, J. Zhang, X. Yu, X.-D. Guo, B.-H. Zhong, Y.-G. Guo, *Adv. Mater.* (2018) 1803765.
- [54] Y. Cai, X. Cao, Z. Luo, G. Fang, F. Liu, J. Zhou, A. Pan, S. Liang, *Adv. Sci.* 5 (2018) 1800680.
- [55] C. Wang, D. Du, M. Song, Y. Wang, F. Li, *Adv. Energy Mater.* 9 (2019) 1900022.
- [56] Y.-Y. Wang, B.-H. Hou, J.-Z. Guo, Q.-L. Ning, W.-L. Pang, J. Wang, C.-L. Lü, X.-L. Wu, *Adv. Energy Mater.* 8 (2018) 1703252.
- [57] F. Wang, N. Zhang, X. Zhao, L. Wang, J. Zhang, T. Wang, F. Liu, Y. Liu, L.-Z. Fan, *Adv. Sci.* 6 (2019) 1900649.
- [58] D. Chao, C.-H.M. Lai, P. Liang, Q. Wei, Y.-S. Wang, C.R. Zhu, G. Deng, V.V.T. Doan-Nguyen, J. Lin, L. Mai, H.J. Fan, B. Dunn, Z.X. Shen, *Adv. Energy Mater.* 8 (2018) 1800058.
- [59] Y. Jiang, X. Zhou, D. Li, X. Cheng, F. Liu, Y. Yu, *Adv. Energy Mater.* 8 (2018) 1800068.
- [60] Y. Liu, N. Zhang, F. Wang, X. Liu, L. Jiao, L.-Z. Fan, *Adv. Funct. Mater.* 28 (2018) 1801917.
- [61] J. Peng, J. Wang, H. Yi, W. Hu, Y. Yu, J. Yin, Y. Shen, Y. Liu, J. Luo, Y. Xu, P. Wei, Y. Li, Y. Jin, Y. Ding, L. Miao, J. Jiang, J. Han, Y. Huang, *Adv. Energy Mater.* 8 (2018) 1702856.
- [62] Q. Ni, Y. Bai, Y. Li, L. Ling, L. Li, G. Chen, Z. Wang, H. Ren, F. Wu, C. Wu, *Small* 14 (2018) 1702864.
- [63] P. Wei, Y. Liu, Y. Su, L. Miao, Y. Huang, Y. Liu, Y. Qiu, Y. Li, X. Zhang, Y. Xu, X. Sun, C. Fang, Q. Li, J. Han, Y. Huang, *ACS Appl. Mater. Interfaces* 11 (2019) 3116–3124.
- [64] C. Chen, Y. Wen, X. Hu, X. Ji, M. Yan, L. Mai, P. Hu, B. Shan, Y. Huang, *Nat. Commun.* 6 (2015) 6929.
- [65] Y. Fang, X.-Y. Yu, X.W.D. Lou, *Adv. Mater.* 30 (2018) 1706668.
- [66] L. Liang, C. Wu, X. Sun, X. Sun, L. Hou, J. Sun, C. Yuan, *Adv. Mater. Interfaces* 4 (2017) 1700382.
- [67] L. Li, M. Xu, Q. Yao, Z. Chen, L. Song, Z. Zhang, C. Gao, P. Wang, Z. Yu, Y. Lai, *ACS Appl. Mater. Interfaces* 8 (2016) 30879–30889.
- [68] T. Jin, Y. Liu, Y. Li, K. Cao, X. Wang, L. Jiao, *Adv. Energy Mater.* 7 (2017) 1700087.
- [69] L. Liang, X. Sun, C. Wu, L. Hou, J. Sun, X. Zhang, C. Yuan, *ACS Appl. Mater. Interfaces* 10 (2018) 5498–5510.
- [70] M. Chen, D. Cortie, Z. Hu, H. Jin, S. Wang, Q. Gu, W. Hua, E. Wang, W. Lai, L. Chen, S.-L. Chou, X.-L. Wang, S.-X. Dou, *Adv. Energy Mater.* 8 (2018) 1800944.
- [71] J.-Y. Hwang, J. Kim, T.-Y. Yu, Y.-K. Sun, *Adv. Energy Mater.* 9 (2019) 1803346.
- [72] F. Kong, X. Fan, A. Kong, Z. Zhou, X. Zhang, Y. Shan, *Adv. Funct. Mater.* 28 (2018) 1803973.
- [73] M. Zarrabeitia, L. Gomes Chagas, M. Kuenzel, E. Gonzalo, T. Rojo, S. Passerini, M.A. Munoz-Marquez, *ACS Appl. Mater. Interfaces* 11 (2019) 28885–28893.
- [74] A. Jin, M.-J. Kim, K.-S. Lee, S.-H. Yu, Y.-E. Sung, *Nano Res.* 12 (2019) 695–700.
- [75] Y.G. Guo, J.Y. Liang, X.D. Zhang, X.X. Zeng, M. Yan, Y.X. Yin, S. Xin, W.P. Wang, X.W. Wu, J.L. Shi, L.J. Wan, *Angew. Chem. Int. Ed.* (2020), doi:10.1002/anie.201916301.